https://doi.org/10.1016/j.apenergy.2021.116832

Thermo-electrochemical modelling of high temperature methanol-fuelled solid oxide fuel cells

Qidong Xu[a], Lingchao Xia[a], Qijiao He[a], Zengjia Guo[a], Meng Ni[a*]

[a] *Building Energy Research Group, Department of Building and Real Estate, The Hong Kong Polytechnic University, Hung Hom, Kowloon, Hong Kong, China*

Abstract:

Methanol is a promising fuel for the solid oxide fuel cell (SOFC) due to its easy storage and transportation compared with hydrogen. As no thermo-electrochemical modelling study has been conducted on methanol-fuelled SOFC, a 2D model was developed to simulate the methanol decomposition reaction, water gas shift reaction, electrochemical reactions, heat and mass transfer processes in the methanol-fuelled SOFC. After model validation, parametric simulations are performed to investigate the effects of the operating potential, steam to carbon ratio, the inlet temperature and fuel/air flow rates on the performance of SOFCs. At 1073K, the peak power density of methanol-fuelled SOFC is higher than 10000 W m^{-2} with a S/C ratio of 1. In addition, the temperature distribution in SOFC could be remarkably affected by the working conditions due to the chemical/electrochemical reactions and overpotential losses. Large temperature variation (nearly 180 K) between the inlet and outlet of the SOFC is observed mainly due to greatly improved current density at low operating potential. Also, temperature reduction can be achieved by increasing the steam to carbon ratio and gas flow rates (higher than 170 SCCM for air and 0.1 ml min^{-1} for fuel mixture, respectively), which could improve the long-term stability from the perspective of the thermal stress but inevitably lower the efficiency of the SOFC. Meanwhile, higher inlet temperature not only enhances the power output, but improves the uniformity of the cell temperature distribution. Overall, the investigations of the present study could serve as a solid guidance to understand the thermal characteristics of solid oxide fuel cells running on mixture of the steam and methanol.

Keywords: Solid oxide fuel cell; Modeling; Methanol fuel; Carbon suppression; Thermal effects.

* Corresponding author (M. Ni)
Email: meng.ni@polyu.edu.hk; Tel: 852-27664152; Fax: 852-27645131

HIGHLIGHTS:

- A 2D model is developed for the methanol-fuelled SOFC.
- Addition of steam helps inhibit carbon deposition but decreases SOFC performance.
- The temperature distribution in the SOFC is substantially influenced by the operating conditions.
- A higher temperature is beneficial to improve the SOFC power output and temperature uniformity.

Nomenclature

Abbreviation

YSZ	Yttria-stabilized zirconia
LSM	Lanthanum strontium manganate
SOFC	Solid oxide fuel cell
SCCM	Standard cubic centimeters per minute
TPB	Triple-phase boundary
MDR	Methanol decomposition reaction
WGSR	Water gas shift reaction

Roman

c	Concentration of the gas mixture, mol m^{-3}
C_p	Heat capacity, J mol^{-1} K^{-1}
D_{ij}	Binary diffusion coefficient of *i* and *j*, cm^2 s^{-1}
D_{ik}	Knudsen diffusion coefficient of *i*, cm^2 s^{-1}
D_{ij}^{eff}	Effective binary diffusion coefficient of *i* and *j*, cm^2 s^{-1}
E	Equilibrium Nernst potential, V
F	Faraday constant, 96,485 C mol^{-1}
ΔG	Gibbs free energy, kJ mol^{-1}
h	Enthalpy of formation, kJ mol^{-1}
ΔH	Enthalpy change of formation, kJ mol^{-1}
i	Current density, A m^{-2}
i_0	Exchange current density, A m^{-2}
J_i	Molar diffusion flux of species *i*, mol m^{-2} s^{-1}
M_i	Molecular weight of species *i*, kg mol^{-1}
n	Number of electrons transferred per electrochemical reaction
N_i	Molar flux of species *i*, mol m^{-2} s^{-1}
p	(partial) Pressure, Pa
Q_e	Energy source, W m^{-3}
Q_m	Mass source, kg m^{-3} s^{-1}
r	Mean pore radius, m
R	Gas constant, 8.3145 J mol^{-1} K^{-1}
R_r	Rate of chemical reaction, mol m^{-3} s^{-1}
R_i	Rate of generation or consumption of species *i*, mol m^{-3} s^{-1}
S	Entropy, J mol^{-1} K^{-1}
ΔS	Entropy change, J mol^{-1} K^{-1}
S_{TPB}	Specific surface area, m^2 m^{-3}
T	Temperature, K
u	Molar-averaged velocity, m s^{-1}
U	Mass-averaged velocity, m s^{-1}
V	Volume fraction
y_i	Molar fraction of species *i*

Greek letters

α	Charge transfer coefficient
ε	Porosity
η	Polarization, V
κ	Permeability, m^2
λ	Thermal conductivity, W m^{-1} K^{-1}
μ	Dynamic viscosity of gas mixture, Pa s
μ_i	Dynamic viscosity of species *i*, Pa s
ρ	Mass concentration of the mixture or the density, kg m^{-3}
σ	Electrical conductivity, S m^{-1}
τ	Tortuosity

Subscripts

a	Anode
act	Activation
c	Cathode
che	Chemical reaction
ele	Electrochemical reaction
g	Gas mixture
i	Species *i*
l	Ionic phase
s	Electronic phase
sol	Solid phase

Superscripts

eff	Effective
l	Local

1 Introduction

Solid oxide fuel cell (SOFC) is one of the most attractive fuel-to-power devices for converting the chemical energy into the electricity or high value-added chemicals through electrochemical reactions with higher well-to-wheel efficiency than conventional heat-engine plants [1]. SOFCs normally operate at high temperature from 600 ° to 1000 ℃ to maintain sufficient ionic conductivity of the ceramic electrolyte, which can bring various benefits to the fuel cell system, such as the use of low-cost Ni metal catalyst instead of expensive Pt-based catalyst [2]; be free of CO poisoning problem compared to other lower temperature fuel cell (e.g. PEMFC, proton exchange membrane fuel cell) [3], and direct utilization of numerous gaseous fuels such as alkanes hydrocarbon [2], ammonia [4] and dimethyl ether (DME) [5], liquid alcohols like methanol [6], ethanol [3], and solid fuels including activated carbon [7] as well as biomass [8]. In addition, the solid sandwiched-structure with a gas-tight ion-conducting electrolyte of SOFCs enables no NO_x emission and easy CO_2 capture, which is essential for improving the air quality and alleviating global warming [9].

Although hydrogen has been studied as a popular fuel for fuel cells due to its high heating value [10] and no greenhouse gas emission during the electricity generation process [11], the challenges of effective and low-cost hydrogen production, storage and transportation hinder its wide application [12]. Therefore, numerous efforts have been made to develop SOFCs running on other alternative fuels [13]. Among those, methanol might be an optimal candidate due to the various attractive features and properties. Firstly, the direct utilization of methanol in SOFCs could reduce the requirements for the gas cleaning or pre-treatment due to the low level of impurities in commercial-grade methanol [14] (e.g. no sulfur as additive for the safety reason [15]). Besides, thanks to the liquid state of the methanol at atmospheric pressure and normal ambient temperature [16], it is relatively easy to transport, store and distribute methanol, which greatly promotes the applications of the portable SOFC systems such as auxiliary power generation units in transportation and military uses [17]. Meanwhile, methanol is also the convenient carrier for the syngas (CO and H_2 mixture) [18], since methanol could be synthesized from carbon monoxide and hydrogen at a relatively low temperature [19], and could be reformed back to carbon monoxide and hydrogen at the typical operating temperatures of the SOFCs [17]. Most importantly, the methanol-fuelled SOFCs can achieve efficient and carbon-neutral power generation if the hydrogen for methanol synthesis comes from renewable sources [20] or the bio-methanol is derived from biomass fermentation or gasification, benefiting both economy and environment [18].

However, the typical Ni-based anode of SOFC might suffer from graphitic carbon deposition

when methanol is used as a fuel, which could decrease the performance and durability of the SOFC [14]. Fortunately, severe coking by methanol fuel could be thermodynamically less favourable than other hydrocarbons due to the presence of the C-O bond in methanol, instead of the C-C bond like ethanol (C_2H_5OH) [21]. Pure methanol fuelled anode-supported SOFC achieved high power density of 0.6 and 1.3 W cm^{-2} at 650 ° and 800 ℃, respectively, and no visible carbon on the Ni/YSZ (yttria-stabilized zirconia) anode was detected after tests [6]. The SOFC with the Ni/SDC (samarium-doped ceria) anode ran stably up to 160 hours with no degradations in both current density and voltage (0.5 V) when methanol was used as the fuel, demonstrating the higher resistance towards carbon formation [22]. With the same anode material, the stability test conducted by Meng et al. [23] exhibited reasonable stable operation for 60 hours at 0.8 A cm^{-2} and 600 ℃, and no carbon deposited in the active anode layer although small amount of carbon was detected in the anode channel. High current density operation could be one of the most effective thermodynamic strategies to address the coking issue since high concentration of the electrochemical reaction products (carbon dioxide and steam) could suppress carbon formation thermodynamically [21]. If the current density is high enough, durable operation of dry methane fuelled SOFC could be achieved without carbon deposition [24]. Therefore, according to the Cimenti et al [14], the long-term durability should be tested under low current density or OCV (open circuit voltage) in order to evaluate the coking resistance of SOFC anode. For example, deposited carbon was observed on the Ni-YSZ anode after 12 hours' operation with pure methanol at OCV condition, which subsequently leading to severe delamination of the electrode from the electrolyte [25]. As the SOFC system needs to operate under various working conditions in practice such as zero output situation [14], coking formation could be an issue for pure methanol fuelled SOFC with Ni-based anode [17].

Apart from incorporating the high oxygen storage capacity doped-ceria into the ionic phase of the anode [14], a number of strategies were developed to inhibit the carbon deposition on the Ni-based anode for methanol fuelled SOFC, such as the modification of the Ni-based anode with other metals (copper [26], palladium [27], molybdenum [28], and cobalt [29]) or the addition of the coke tolerant basic oxides (La_2O_3, Sm_2O_3 [30], NbO_x [31], Pr_4O_7 and Pr_6O_{11} [32]). However, due to complicated manufacturing procedures, higher cost and relatively lower catalytic activity, these modification approaches are unlikely to be used for the commercially practical applications. One simplest and effective thermodynamic method to tackle the coking issue is to supply enough oxygen carrier agent to the pure methanol fuel, such as the steam [33]. According to the literature, the deposited carbon in the methanol-fuelled SOFCs may be generated mainly from the Boudouard reaction (Eq. (1)) [26]. The supply of steam in the fuel

stream could promote water gas shift reaction (WGSR, Eq. (2)) to reduce the partial pressure of the carbon monoxide and produce more hydrogen, or react with deposited carbon to form the hydrogen and carbon monoxide (Eq. (3)), eventually preventing carbon formation. Laosiripojana et al. [34] found no carbon formation when the methanol and steam mixture with the ratio of 1.0/3.0 was supplied to the Ni/YSZ catalyst at 1000 ℃. The stability test of the Ni/YSZ anode SOFC operating on the mixture of methanol and steam with the ratio of 1.0/2.0 conducted by Ru et al. [35] achieved a stable output up to 120 hours at a current density of 0.221 A cm^{-2} and at 750 ℃.

$$2CO(g) \leftrightarrow CO_2(g) + C(s) \quad (1)$$

$$CO + H_2O \leftrightarrow CO_2 + H_2 \quad (2)$$

$$H_2O(g) + C(s) \leftrightarrow CO(g) + H_2(g) \quad (3)$$

The above-mentioned studies demonstrate the feasibility of strategies for suppressing carbon formation in methanol fuelled SOFC with Ni-based anode, especially the strategy of supplying sufficient steam to the fuel stream. Although sufficient steam could inhibit carbon formation, excess steam could lower the performance of the SOFC system [36]. Besides, performance and durability of methanol fuelled SOFC could be substantially influenced by the use of steam in the anode. This is because the endothermic internal reforming or decomposition reaction of the methanol would cause the local cooling and result in significant temperature gradients, although the electrochemical reactions and the overpotential losses tend to generate heat [37]. Therefore, highly coupled fluid flow, chemical/electrochemical reactions and heat/mass transfer processes really complicate the temperature field inside the cell, which could induce thermal stress resulting from the temperature gradient and the mismatch of the thermal expansion coefficient (TEC) [38]. Meanwhile, the local lower temperature might thermodynamically favour carbon formation in methanol fuelled SOFC [17]. For stable and efficient operation of methanol fuelled SOFC, a comprehensive understanding of the chemical/electrochemical reactions as well as heat and mass transfer is essential for identifying suitable operating conditions. However, although the thermal behaviour of the SOFCs has been extensively studied, no thermo-electrochemical model has been reported for SOFC running on methanol and steam mixture. The temperature field and the interplay of various operation parameters have not been understood yet.

In this work, the 2D numerical model from the previous research [39] is extended to fully describe the performance and the thermal behaviours of the tubular SOFC operating on the methanol/steam fuel with the typical Ni/YSZ-YSZ-YSZ/LSM configuration without

considering the carbon formation due to the relevant experimental research as well as the operating conditions adopted in present study. The results of the modeling are compared with the experimental data [6] for model validation. The thermal coupling of the methanol conversion process and the electrochemical reactions of the carbon monoxide as well as the hydrogen are conducted in detail to examine the effects of the operating conditions (applied potential and inlet temperature) and the fuel conditions (fuel composition and flow rates) on the power output and temperature distribution of the SOFC.

2 Model development

2.1 Simulation assumptions and working principles

In this study, the mixture of H_2O/CH_3OH with various molar ratios (steam to carbon ratio: S/C ratio) is supplied to the SOFC anode channel for power generation. The transport and reaction processes in the anode-supported SOFC is shown in Fig. 1. The computational domain includes five components, involving anode channel, porous Ni/YSZ composite anode, gas-tight YSZ ceramic electrolyte, porous YSZ/LSM composite cathode, and the cathode channel based on the experimental work studied by Jiang et al [6]. Note that interconnect rib is not included in the geometry of the fuel cell due to the fact that 2D model is conducted in this simulation work. Because the interconnect rib is an important component for the integrity of the fuel cell, which could significantly affect the gas transport, chemical reactions and thus the performance of the SOFCs, rib effect could be considered in the future 3D simulation work. In addition, there are some modifications of the structural dimensions in the current work compared to our previous study [39], and typical parameters used in this simulation work are listed in Table 1.

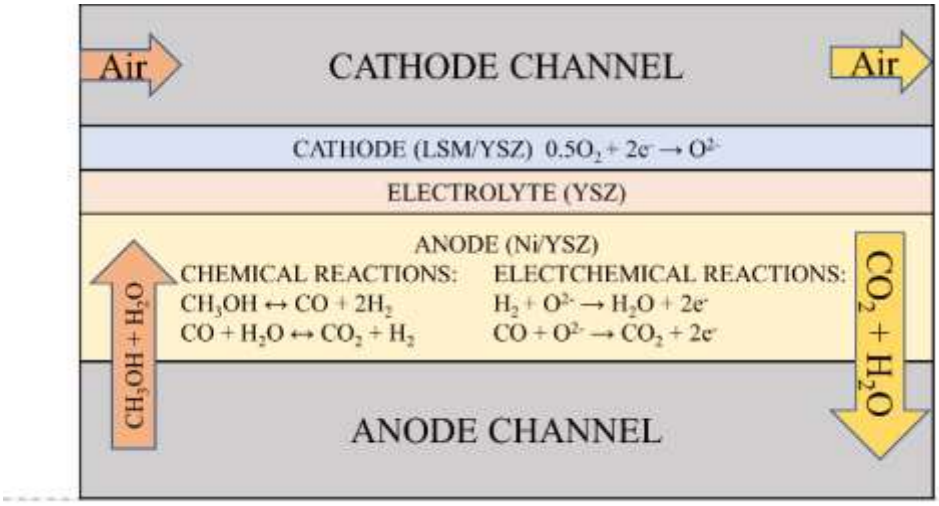

Fig. 1. Schematic of the anode-supported SOFC operating on the methanol and steam mixture.

Table 1 Model parameters [6,9,39,40].

Parameter	Expression or value	Unit
Bulk electronic conductivity		
Nickel	$3.27 \times 10^6 - 1065.3 \times T$	S m^{-1}
LSM	$4.2 \times 10^7/T \times e^{\frac{-1150}{T}}$	S m^{-1}
Bulk ionic conductivity		
YSZ	$3.34 \times 10^4 \times e^{\frac{-10300}{T}}$	S m^{-1}
Porosity		
Cathode	0.46	
Anode	0.46	
Permeability		
Cathode	1.76×10^{-11}	m^2
Anode	1.76×10^{-11}	m^2
S_{TPB}		
Cathode	3.33×10^5	m^2 m^{-3}
Anode	2.66×10^5	m^2 m^{-3}
Thickness		
Anode channel	2	mm
Anode	0.6	mm
Electrolyte	0.01	mm
Cathode	0.1	mm
Cathode channel	2	mm
Cell length	6	cm
Tortuosity of porous electrode	3	

During operation, the ambient air and the steam/methanol mixture are supplied to the air and the fuel gas channels, respectively. Methanol can be easily converted into the syngas under the catalytic effect of the Ni metal via the methanol decomposition reaction (MDR, Eq. (4)) as the methanol fuel diffuses into the anode. Meanwhile, carbon monoxide tends to react with sufficient steam supplied or generated from the electrochemical oxidation of hydrogen (Eq. (5)) to produce more hydrogen through the WGSR (Eq. (2)). Although methane might be produced from methanol decomposition, it is negligible according to the previous experimental research. Besides, although a certain amount of methane could be produced from the methanation reaction in practice, due to the requirements of a high pressure and a relatively lower temperature for methanation process [34], the methane production and/or reforming reaction is neglected in present work.

$$CH_3OH \leftrightarrow CO + 2H_2 \quad (4)$$

The produced hydrogen and the remaining carbon monoxide are oxidized to form the steam and carbon dioxide (Eqs. (5) and (6)) at the triple phase boundary (TPB) by the O^{2-} transported from the cathode where the oxygen molecules are reduced (Eq. (7)) at TPB sites by the electrons transferred from the anode through the external circuit.

$$H_2 + O^{2-} \rightarrow H_2O + 2e^- \quad (5)$$

$$CO + O^{2-} \rightarrow CO_2 + 2e^- \quad (6)$$

$$0.5O_2 + 2e^- \rightarrow O^{2-} \quad (7)$$

Based on the mechanism demonstrated above, the following assumptions are adopted.

(1) Only electrochemical oxidations of hydrogen and carbon monoxide are considered;

(2) The ionic/electronic phases are assumed to be continuous and homogeneous;

(3) The active catalyst sites for chemical/electrochemical reactions are uniformly distributed in the electrodes and the nickel metal will not be re-oxidized by the steam;

(4) Gases are assumed to be ideal gases;

(5) The laminar flow is adopted in the fluid flow since Reynolds number of the fuel stream or air stream is relatively low;

(6) The heat radiation effect is assumed to be negligible.

2.2 Governing equations

According to the processes of the SOFC, the thermo-electrochemical model consists of five sub-models in the present study.

2.2.1 Chemical reaction model

Reaction rates and related heat could be calculated by the chemical reaction model. MDR and WGSR are expected to take place in the anode layer based on the assumptions, while these reactions in the anode channel could be negligible due to the lack of catalyst [41]. The reaction rates for MDR (R_{MDR}) and reversible WGSR (R_{WGSR}) can be calculated as shown below:

The MDR [42]:

$$R_{MDR} = k_D p^l_{CH_3OH} E_{qD} \quad (8)$$

$$E_{qD} = 1 - \frac{p^l_{CO}\left(p^l_{H_2}\right)^2}{K_{eq,D} p^l_{CH_3OH}} \quad (9)$$

$$K_{eq,D} = 1.718 \times 10^{14} \exp\left(-\frac{95419}{RT}\right) \quad (10)$$

The WGSR [43]:

$$R_{WGSR} = k_{sf}\left(p^l_{H_2O} p^l_{CO} - \frac{p^l_{H_2} p^l_{CO_2}}{K_{ps}}\right) \quad (11)$$

$$k_{sf} = 0.0171 \exp\left(-\frac{103191}{RT}\right) \quad (12)$$

$$K_{ps} = \exp\left(-0.2935Z^3 + 0.6351Z^2 + 4.1788Z + 0.3169\right) \quad (13)$$

$$Z = \frac{1000}{T(K)} - 1 \quad (14)$$

where the k_D is the tuning parameter used for model validation; R and T denote the universal gas constant and temperature, respectively; p_i^l represents the local partial pressure of species i.

According to thermodynamics, the enthalpy changes of formation (ΔH) in the form of heat

absorption or generation will be accompanied with the occurrences of the chemical reactions. Therefore, the chemical heat changes (Q_{che}) associated with the MDR and WGSR could be determined by Eq. (15), involving the heat consumption by the endothermic MDR (ΔH_{MDR}, Eq. (16)) and heat generation from the exothermic WGSR (ΔH_{WGSR}, Eq. (17)),

$$Q_{che} = R_{MDR}\Delta H_{MDR} + R_{WGR}\Delta H_{WGSR} \quad (15)$$

$$\Delta H_{MDR} = 2h_{H_2} + h_{CO} - h_{CH_3OH} \quad (16)$$

$$\Delta H_{WGSR} = h_{CO_2} + h_{H_2} - h_{CO} - h_{H_2O} \quad (17)$$

where h_i is the enthalpy of formation of the species i, which can be calculated by the definition of the enthalpy (Eq. (18)).

$$h(T) = h(T_0) + \int_{T_0}^{T} C_p(T)\, dT \quad (18)$$

2.2.2 Electrochemical reaction model

The electricity power and the irreversible heat produced from electrochemical oxidation and reduction reactions could be described by the electrochemical reaction model. In electrochemistry, the general Butler-Volmer (BV) equation is used to link the current density with the activation overpotential (η_{act}). In the present study, hydrogen and carbon monoxide participate in the electrochemical reactions as fuels for the SOFC. Therefore, the current density (i) produced from Eqs. (5), (6) and (7) could be determined by:

$$i = i_0 \left\{ \exp\left(\frac{\alpha n F \eta_{act}}{RT}\right) - \exp\left(\frac{-(1-\alpha) n F \eta_{act}}{RT}\right) \right\} \quad (19)$$

where i_0 is the exchange current density. In the previous experimental research, the rate of CO electrochemical oxidation is about 0.32-0.52 times that of H_2 electrochemical oxidation rate. Thus, the i_0 for H_2, CO and O_2 are set to be 5300 A m^{-2}, 3000 A m^{-2} and 2000 A m^{-2}, respectively. More detailed information can be found in ref. [39]. n, α and F are the number of electrons generated from a single electrochemical reaction, the charge transfer coefficient, and the Faraday constant, respectively. The operating potential (V) can be given by the subtraction of activation and ohmic overpotential losses from thermodynamic equilibrium potential (E, Nernst potential):

$$V = E - \eta_{act,a} - \eta_{act,c} - \eta_{ohmic} \quad (20)$$

here η_{ohmic} signifies the overpotential related to the transport of the ion and electron; E can be expressed by [44,45]:

$$E_{H_2} = E_{H_2}^{T} + \frac{RT}{2F}\left[\frac{p_{H_2}^{l}\left(p_{O_2}^{l}\right)^{0.5}}{p_{H_2O}^{l}}\right] \quad (21)$$

$$E_{CO} = E_{CO}^{T} + \frac{RT}{2F}\left[\frac{p_{CO}^{l}\left(p_{O_2}^{l}\right)^{0.5}}{p_{CO_2}^{l}}\right] \tag{22}$$

$$E_{H_2}^{T} = 1.253 - 0.00024516T \tag{23}$$

$$E_{CO}^{T} = 1.46713 - 0.0004527T \tag{24}$$

here, concentration overpotentials have already been included due to the fact that local partial pressures of the relevant species are used for the calculations of Eqs. (21) and (22).

Besides, the Ohm's law is used to describe the ohmic potential losses (η_{ohmic}):

$$i_l = -\sigma_l^{eff}\nabla(\emptyset_l) \tag{25}$$

$$i_s = -\sigma_s^{eff}\nabla(\emptyset_s) \tag{26}$$

where $\emptyset_l$ and $\emptyset_s$ represent the ionic and electronic phase potentials, respectively; σ_l^{eff} and σ_s^{eff} denote the effective conductivities of the ion and electron in the electrodes, which can be determined by the intrinsic conductivities of the materials and the volume fractions of the ionic (V_l) and electronic (V_s) phases in the electrodes as well as the tortuosity (τ) of the porous structures [46], as calculated by Eqs. (27) and (28).

$$\sigma_l^{eff} = \sigma_l \cdot \frac{V_l}{\tau_l} \tag{27}$$

$$\sigma_s^{eff} = \sigma_s \cdot \frac{V_s}{\tau_s} \tag{28}$$

The heat will be released during the electrochemical processes, since from the perspective of the thermodynamics, the maximum electricity energy available from the fuel is the Gibbs free energy (ΔG) [2]. Therefore, based on the second law of thermodynamics (Eq. (29)), the heat (Q_{ele}) related to the electrochemical reactions can be written as:

$$T\Delta S = \Delta H - \Delta G \tag{29}$$

$$Q_{ele} = \frac{i_{H_2} T\Delta S_{H_2}}{2F} + \frac{i_{CO} T\Delta S_{CO}}{2F} \tag{30}$$

here, $T\Delta S$ represents irreversible energy loss of the electrochemical reactions, and ΔS is the entropy change of the hydrogen or carbon monoxide electrochemical reactions, which can be determined by [41]:

$$\Delta S_{H_2} = s_{H_2O} - 0.5s_{O_2} - s_{H_2} \tag{31}$$

$$\Delta S_{CO} = s_{CO_2} - 0.5s_{O_2} - s_{CO} \tag{32}$$

where, s_i is the entropy of the species i, which can be calculated by the definition of the entropy (Eq. (33)).

$$s(T) = S(T_0) + \int_{T_0}^{T} \frac{C_p(T)}{T} dT \tag{33}$$

2.2.3 Computational fluid dynamics model

The CFD model is used to simulate the gas flow in both channels and porous electrodes. The continuity equation (Eq. 34) and the classic NS (Navier-Stokes) equation (Eq. (35)) at steady state are applied in the fuel and gas channels [41].

Mass conservation:

$$\rho\nabla \cdot U = 0 \tag{34}$$

Momentum conservation:

$$\rho(U \cdot \nabla) \cdot U = -\nabla p + \nabla \cdot [\mu(\nabla U + \nabla U^T)] \tag{35}$$

Owing to the porous structure of the electrodes and the mass exchange between the anode and cathode because of the anion transfer, a source term is included in the continuity equation to account for the mass transfer from the cathode to the anode (Eq. 36). The Brinkman equations, the modified NS equations with the Darcy' term, are utilized to describe the momentum conservation in the porous electrodes (Eq. 37) [36]:

Mass conservation:

$$\rho\nabla \cdot U = Q_m \tag{36}$$

Momentum conservation:

$$\frac{1}{\varepsilon}\rho(U \cdot \nabla) \cdot U\frac{1}{\varepsilon} = -\nabla p + \nabla \cdot \left[\mu\frac{1}{\varepsilon}(\nabla U + \nabla U^T) - \frac{2}{3}\mu\frac{1}{\varepsilon}(\nabla \cdot U)\right] - \left(\mu\kappa^{-1} + \frac{Q_m}{\varepsilon^2}\right)U \tag{37}$$

where κ and ε are the permeability and the porosity of the porous media, respectively; p and U are the pressure and mass average velocity of the gas mixture, respectively; the source term Q_m denotes the oxygen transferred from cathode to the anode; μ represents the dynamic viscosity of the gas mixture and can be written as :

$$\mu = \sum_{i=1}^{n} \frac{y_i\mu_i}{\sum_{j=1}^{n}(y_i\sqrt{\frac{M_j}{M_i}})} \tag{38}$$

where M_i and y_i are the molecular weight and molar fraction of species i, respectively, and the dynamic viscosity for each gas (μ_i) can be found in Table 2.

Table 2 Dynamic viscosity of gas species [47].

μ_i	Value	Unit
CO	$(23.811 + 0.53944 \times T - 1.5411 \times 10^{-4} \times T^2) \times 10^{-7}$	Pa s
CO_2	$(11.811 + 0.49838 \times T - 1.0851 \times 10^{-4} \times T^2) \times 10^{-7}$	Pa s
H_2	$(27.758 + 0.212 \times T - 3.28 \times 10^{-5} \times T^2) \times 10^{-7}$	Pa s
H_2O	$(-36.826 + 0.429 \times T - 1.62 \times 10^{-5} \times T^2) \times 10^{-7}$	Pa s
CH_3OH	$(-14.236 + 0.38935 \times T - 6.2762 \times 10^{-5} \times T^2) \times 10^{-7}$	Pa s
O_2	$(44.224 + 0.562 \times T - 1.13 \times 10^{-4} \times T^2) \times 10^{-7}$	Pa s
N_2	$(42.606 + 0.475 \times T - 9.88 \times 10^{-5} \times T^2) \times 10^{-7}$	Pa s

2.2.4 Mass transfer model

Mass transfer model is employed to calculate the concentration of each uncharged gaseous species in the SOFC due to various complicated processes, involving mixing, convection, and diffusion etc. Therefore, the molar conservation equations of species *i* at steady state are shown below:

In the channels:

$$\nabla \cdot J_i + c(u \cdot \nabla) y_i = 0 \tag{39}$$

In the electrodes:

$$\nabla \cdot J_i + c(u \cdot \nabla) y_i = R_i \tag{40}$$

where c is the gas mixture concentration; J_i represents the molar diffusion flux of species i;, and R_i is the mole change rate of species i as a result of the electrochemical/chemical processes; u denotes the molar average velocity of the gas mixture.

Diffusion flux of species i in Eqs. (39) and (40) is calculated by the Stefan-Maxwell approach [48]. The molecular diffusion or continuum diffusion plays a major role in the fuel or air channel [49], while in the porous electrodes, both molecular diffusion and Knudsen diffusion need to be considered [50]. Therefore, the steady-state diffusion models are described by:

In the channels:

$$\sum_{j=1, j\neq i}^{n} \frac{y_j N_i - y_i N_j}{D_{ij}} = -c \frac{dy_i}{dx} \tag{41}$$

In the electrodes:

$$\sum_{j=1, j\neq i}^{n} \frac{y_j N_i - y_i N_j}{D_{ij}^{eff}} = -c \frac{dy_i}{dx} \tag{42}$$

here N_i denotes the molar flux of species i; D_{ij} is the binary diffusion coefficient of species i and j, which can be given by Fuller et al. expression (Eq. (43)) [51]; D_{ij}^{eff} is the effective binary diffusion coefficient of species i and j considering the molecular diffusion and the Knudsen diffusion with the correction of microstructures of the porous electrodes (Eq. (44)) [52],

$$D_{ij} = \frac{0.00143 T^{1.75}}{2p\left(v_i^{1/3} + v_j^{1/3}\right)^2} \left(\frac{1}{M_i} + \frac{1}{M_j}\right)^{1/2} \tag{43}$$

$$D_{ij}^{eff} = \frac{\varepsilon}{\tau} \left(\frac{1}{D_{ij}} + \frac{1}{D_{ik}}\right)^{-1} \tag{44}$$

here v_i represents special molecule diffusion volume, which can be found in the Table 3.

Knudsen diffusion coefficient (D_{ik}) can be calculated based on the kinetic theory [53], as expressed below:

$$D_{ik} = \frac{2}{3} r \sqrt{\frac{8RT}{\pi M_i}} \tag{45}$$

here r represents the mean pore radius of the electrode.

Table 3 Special molecule diffusion volume of each species [54].

v_i	Value	Unit
CO	18.0	cm^3
CO_2	26.7	cm^3
H_2	6.12	cm^3
H_2O	13.1	cm^3
CH_3OH	31.25	cm^3
O_2	16.3	cm^3
N_2	18.5	cm^3

2.2.5 Heat transfer model

Heat transfer model is developed to simulate the temperature field in the whole computational domain. The heat transfer processes inside the SOFC are complicated, including the heat generation from the electrochemical reactions, irreversible overpotential loss, and the exothermic WGSR, as well as the heat consumption by endothermic MDR, leading to nonuniform temperature distribution. Therefore, the general energy conservation equations are applied:

In the channels:

$$\rho C_p u \cdot \nabla T + \nabla \cdot \left(-\lambda_g \nabla T\right) = 0 \tag{46}$$

In the electrodes or the electrolyte:

$$\rho C_p u \cdot \nabla T + \nabla \cdot \left(-\lambda_{eff} \nabla T\right) = Q_e \tag{47}$$

$$\lambda_g = \sum_{i=1}^{n} y_i \lambda_i \tag{48}$$

$$C_p = \sum_{i=1}^{n} y_i C_{p,i} \tag{49}$$

$$\lambda_{eff} = (1-\varepsilon)\lambda_{sol} + \varepsilon \lambda_g \tag{50}$$

where λ_{sol} represents the thermal conductivity of the solid structure; the thermal conductivity (λ_g) and the heat capacity (C_p) of the gas mixture can be estimated by the mole fraction averaging (Eqs. (48) and (49) [51,55]; the effective thermal conductivity (λ_{eff}) is determined by the volume fractions of the solid phase and gas phase (Eq. (50)) The thermodynamic properties of the gas species and the solid structure materials can be found in Table 4 and Table 5, respectively.

Q_e (W m^{-3}) is the source term accounting for the heat generation or heat consumption in the SOFC. The source terms to be applied to anode, electrolyte, and cathode are calculated by Eqs. (51), (52) and (53) respectively,

In the anode:

$$Q_e = Q_r + Q_{ele} + i_{H_2}\eta_{act,H_2} + i_{CO}\eta_{act,CO} + \left(\frac{i_l^2}{\sigma_l^{eff}} + \frac{i_s^2}{\sigma_s^{eff}}\right) \quad (51)$$

In the electrolyte:

$$Q_e = \frac{i_l^2}{\sigma_l^{eff}} \quad (52)$$

In the cathode

$$Q_e = \left(i_{H_2} + i_{CO}\right)\eta_{act,O_2} + \left(\frac{i_l^2}{\sigma_l^{eff}} + \frac{i_s^2}{\sigma_s^{eff}}\right) \quad (53)$$

here $i_{H_2}\eta_{act,H_2}$ and $i_{CO}\eta_{act,CO}$ are the heat generated from the activation overpotentials of the electrochemical oxidations of the H_2 and CO, which are applied based on the distributions of the η_{act,H_2} and $\eta_{act,CO}$ in the electrodes; $\frac{i_s^2}{\sigma_s^{eff}}$ or $\frac{i_l^2}{\sigma_l^{eff}}$ represents the ohmic heat due to the resistances of the electron or ion, which will be applied to corresponding components.

Table 4 Thermodynamic properties of the gas species [47].

Gas species	Value	Unit
λ_i		
CO	$0.00158 + 8.2511 \times 10^{-5} \times T - 1.9081 \times 10^{-8} \times T^2$	W m^{-1} K^{-1}
CO_2	$-0.012 + 1.0208 \times 10^{-4} \times T - 2.2403 \times 10^{-8} \times T^2$	W m^{-1} K^{-1}
H_2	$0.03591 + 4.5918 \times 10^{-4} \times T - 6.4933 \times 10^{-8} \times T^2$	W m^{-1} K^{-1}
H_2O	$0.00053 + 4.7093 \times 10^{-5} \times T + 4.9551 \times 10^{-8} \times T^2$	W m^{-1} K^{-1}
CH_3OH	$-0.007797 + 4.167 \times 10^{-5} \times T + 1.217 \times 10^{-7} \times T^2$	W m^{-1} K^{-1}
O_2	$0.00121 + 8.6157 \times 10^{-5} \times T - 1.3346 \times 10^{-8} \times T^2$	W m^{-1} K^{-1}
N_2	$0.00309 + 7.593 \times 10^{-5} \times T - 1.1014 \times 10^{-8} \times T^2$	W m^{-1} K^{-1}
$C_{p,i}$		
CO	$29.556 - 6.5807 \times 10^{-3} \times T + 2.013 \times 10^{-5} \times T^2 - 1.2227 \times 10^{-8} \times T^3 + 2.2617 \times 10^{-12} \times T^4$	J mol^{-1} K^{-1}
CO_2	$27.437 + 4.2315 \times 10^{-2} \times T - 1.9555 \times 10^{-5} \times T^2 + 3.9968 \times 10^{-9} \times T^3 - 2.9872 \times 10^{-13} \times T^4$	J mol^{-1} K^{-1}
H_2	$25.399 + 2.1078 \times 10^{-2} \times T - 3.8549 \times 10^{-5} \times T^2 + 3.188 \times 10^{-8} \times T^3 + 8.7585 \times 10^{-12} \times T^4$	J mol^{-1} K^{-1}
H_2O	$33.933 - 8.4186 \times 10^{-3} \times T + 2.9906 \times 10^{-5} \times T^2 - 1.7825 \times 10^{-8} \times T^3 + 3.6934 \times 10^{-12} \times T^4$	J mol^{-1} K^{-1}
CH_3OH	$40.046 - 3.8287 \times 10^{-2} \times T + 2.4529 \times 10^{-4} \times T^2 - 2.1679 \times 10^{-7} \times T^3 + 5.9909 \times 10^{-11} \times T^4$	J mol^{-1} K^{-1}
O_2	$29.526 - 8.8999 \times 10^{-3} \times T + 3.8083 \times 10^{-5} \times T^2 - 3.2629 \times 10^{-8} \times T^3 + 8.8607 \times 10^{-12} \times T^4$	J mol^{-1} K^{-1}
N_2	$29.342 - 3.5395 \times 10^{-3} \times T + 1.0076 \times 10^{-5} \times T^2 - 4.3116 \times 10^{-9} \times T^3 + 2.5935 \times 10^{-13} \times T^4$	J mol^{-1} K^{-1}

Table 5 Thermodynamic properties of the materials [56,57].

Material	C_p, J mol^{-1} K^{-1}	λ, W m^{-1} K^{-1}	ρ, kg m^{-3}
Ni/YSZ	390	6.23	6870
YSZ	525	2.57	6086

YSZ/LSM	398	3.47	3814.8

2.3 Numerical methods and validation

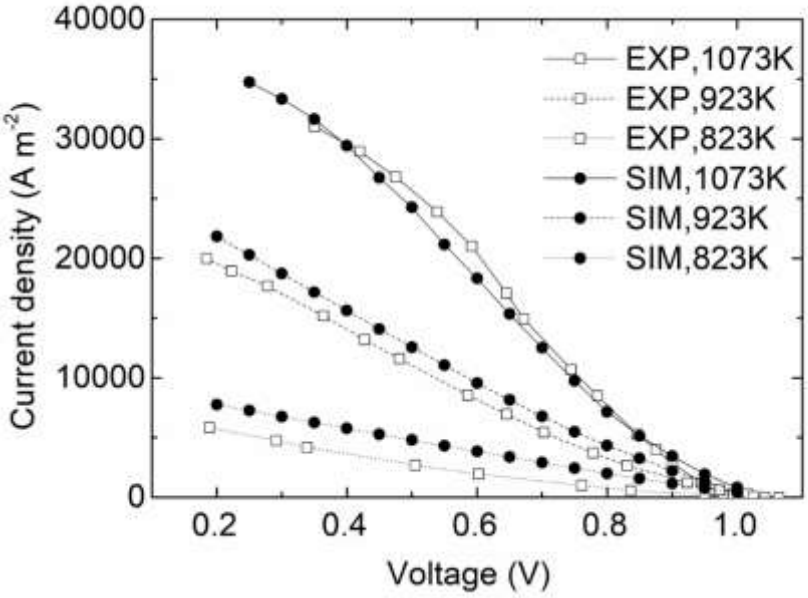

Fig. 2 Model validation of the model.

The model is developed and calculated by the commercial software COMSOL using the Finite Element Method. The mesh of 52 000 elements is selected to achieve grid-independence of the results. The numbers of the mesh elements for cell length, anode channel, anode, electrolyte, cathode, and cathode channel widths are 200, 30, 150, 10, 40, and 30, respectively. The model was validated by comparing with experimental results [6] in our earlier work [39] (Fig. 2). The parametric computations are conducted afterwards to investigate the effects of the operating conditions on performance and the thermal characteristics of the cell. The operating conditions are summarized in Table 6.

Table 6 Working parameters for parametric simulations.

Parameters	Value	Unit
Anode fuel flow rate (liquid)	0.05-1	ml min^{-1} (std)
Cathode gas flow rate	10-600	SCCM
S/C ratio at the anode inlet	H_2O/CH_3OH (1/1 – 8/1)	
Cathode inlet gas composition	O_2/N_2 (21%/79%)	
Inlet temperature	898-1173	K
Operation potential	0.2-0.9	V
Operation pressure	1	atm

3 Results and discussion

3.1 The effects of the operating voltage

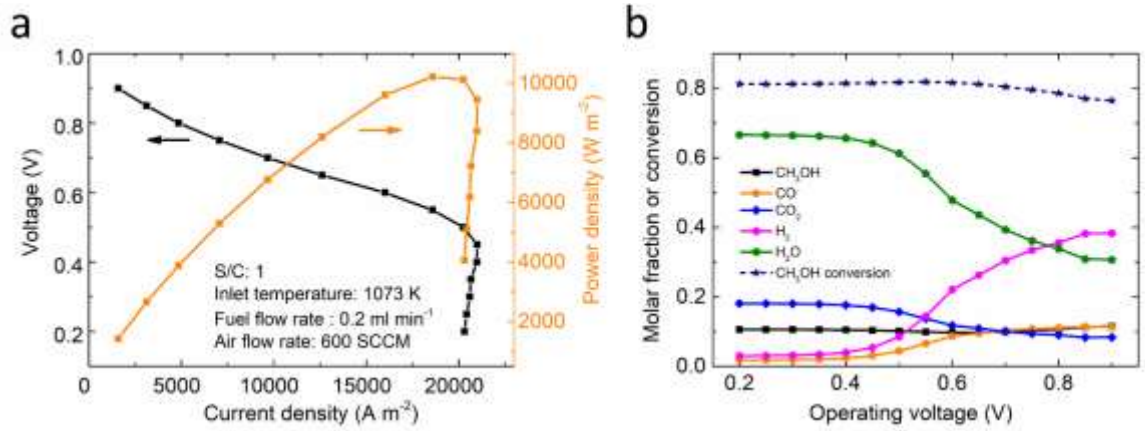

Fig. 3. The effects of the operating voltage on: (a) current density and power density; (b) the anode gas fraction at the outlet and the methanol conversion.

Simulations are conducted at an inlet temperature of 1073K to investigate the effects of operating voltage on the performance of the SOFC running on the steam/methanol mixture with molar ratio of 1/1. The calculated current density shown in Fig. 3a is found to be significantly affected by the operating voltage changing from 0.9 V to 0.2 V when the flow rates for fuel and air are 0.2 ml min^{-1} and 600 SCCM, respectively.

As expected, the current density is greatly improved from 1585 A m^{-2} to 20997 A m^{-2} when the voltage decreases from 0.9 V to 0.45 V. Meanwhile, a peak power density of 10220 W m^{-2} is achieved at 0.55 V, which is much higher than that (usually less than 1000 W m^{-2}) of typical room temperature direct methanol fuel cells (DMFCs) [58,59]. Besides, the gas composition is also greatly influenced. Highly consumptions of the direct fuels (carbon monoxide and hydrogen) for electrochemical reactions and increased products (steam and carbon dioxide) are observed in Fig. 3b at a high current density. As a result, the enhanced consumption of hydrogen and carbon monoxide fuel help improve the methanol conversion slightly to be above 0.8 as the voltage is decreased from 0.9 V to 0.6 V. However, increased amount of the gas molar number because of the decomposition reaction, and the relatively low methanol concentration limit the further increase in methanol conversion, as the voltage is further decreased from 0.6 V to 0.2 V (Fig. 3b). As the methanol conversion is not further increased and the syngas fuel is consumed by electrochemical reactions, the current density is found to decrease slightly with further decrease in operating voltage from about 0.45 V to 0.2 V (Fig. 3a).

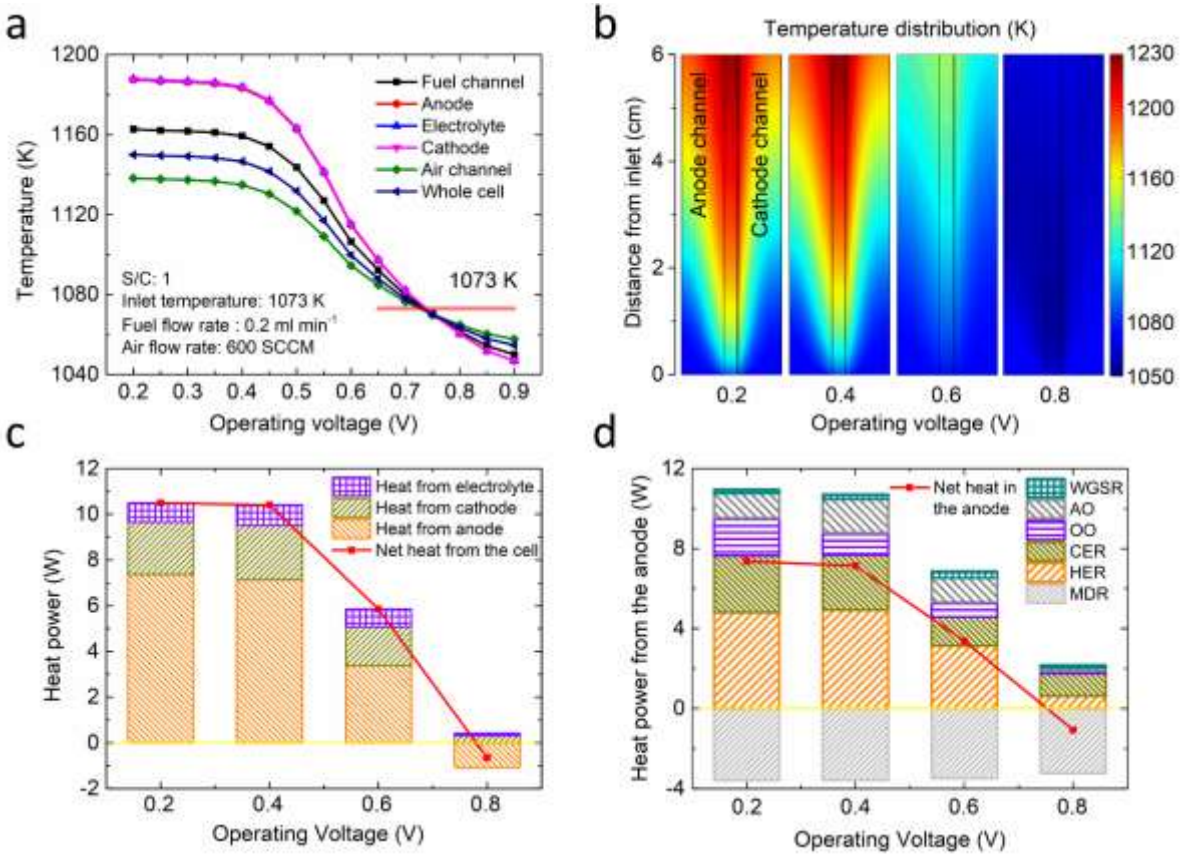

Fig. 4. The effects of the operating voltage on: (a) average temperature of each component; (b) temperature distribution; (c) heat source of each component; (d) heat source of the anode (AO: activation overpotential; OO: ohmic overpotential; CER: carbon monoxide electrochemical reaction; HER: hydrogen electrochemical reaction).

The operating voltage also has a strong influence on the cell temperature distribution, as illustrated in Fig. 4a and b. The average temperature of each component is found to increase with decreasing voltage due to the increased rate of heat generation from electrochemical reactions and various overpotential losses (Fig. 4c and d). More importantly, when the operating voltages are 0.2 V and 0.4 V, the temperature of the fuel cell is increased significantly along the length of the cell, as shown in Fig. 4a, which is mainly because of the highly enhanced exothermic processes at lower operating voltage (Fig. 4c) and also the heat convection effect by the gas supply. Therefore, the huge difference of the temperature within the fuel cell should be avoided in the practical operation since higher temperature gradient could induce the unbearable thermal stress and even the failure of the whole fuel cell. One interesting phenomenon from Fig. 4a is that the average temperatures of anode, cathode and electrolyte are nearly same. This is because the high thermal conductivities of the solid materials ensure fast heat conduction. In addition, due to endothermic methanol decomposition reaction, the thermal neutral status can be attained between 0.7 V to 0.8 V (Fig. 4a), which

indicates that the total heat generation rate is equal to the rate of heat consumption by the MDR (Fig. 4c and d). Despite of the overall thermal balance, the highly non-uniform temperature distribution in the SOFC could cause concerns for long term performance and durability. For example, a cooling spot near the inlet can be seen at a potential of 0.8 V in Fig. 4b, which is consistent with the operation of the SOFC running on mixture of the methane and the steam [60]. The temperature of this region is found lower than the inlet temperature due to the high rate of endothermic MDR and relatively low electrochemical reaction rate, which can cause local low cell performance and large thermal stress.

3.2 The effects of the steam to carbon ratio

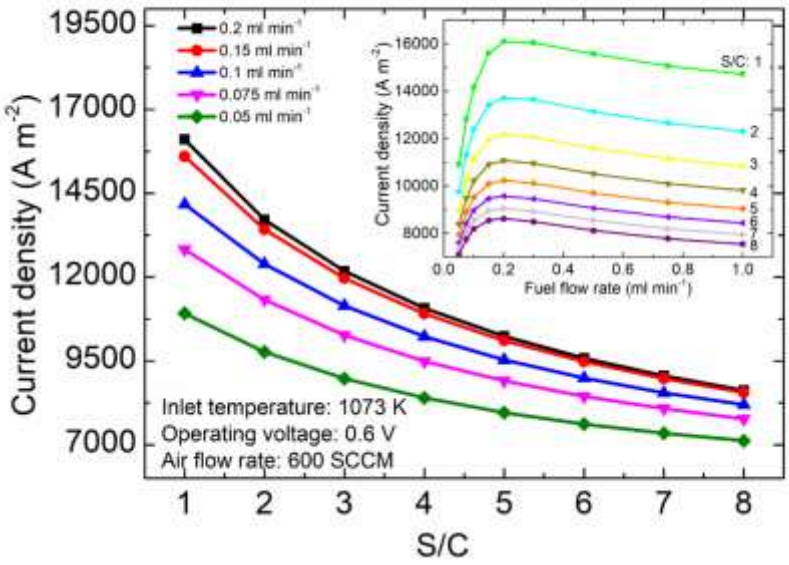

Fig. 5. The effect of the S/C ratio on current density.

To prevent carbon deposition in the SOFC anode, steam is supplied with the methanol fuel. Different amounts of steam with the steam to carbon (S/C) ratio from 1 to 8 are supplied to the anode under different fuel flow rates at the inlet temperature of 1073 K and the operating potential of 0.6 V when the air flow rate is 600 SCCM. From Fig. 5, it is clear to observe that the current densities are decreased with increasing S/C ratio at various fuel flow rates, which is mainly due to the higher dilution effect on the methanol fuel and the produced syngas fuel (Fig. 6a). On the one hand, the methanol decomposition rate is decreased due to lower methanol concentration (Fig. 6b), causing much less productions of the carbon monoxide and hydrogen for the electrochemical reaction. On the other hand, the produced syngas fuel is also diluted by steam, leading to lower local equilibrium potential and lower current density. Meanwhile, the total heat generation is decreasing due to lower current density as the S/C ratio increases (Fig. 6c), leading to much more uniform temperature distribution in the cell (Fig. 6d). In general,

due to the porous nature of the electrodes, the fraction strengths of compressive stress for the electrodes (e.g. 100 MPa for both NiO/YSZ and LSM/YSZ when the porosity is 0.4 [61]) are much lower than that of the dense electrolyte (e.g. 1 GPa for YSZ [62]). Therefore, more uniform temperature distribution in the electrodes is significantly important for the durability of the SOFCs.

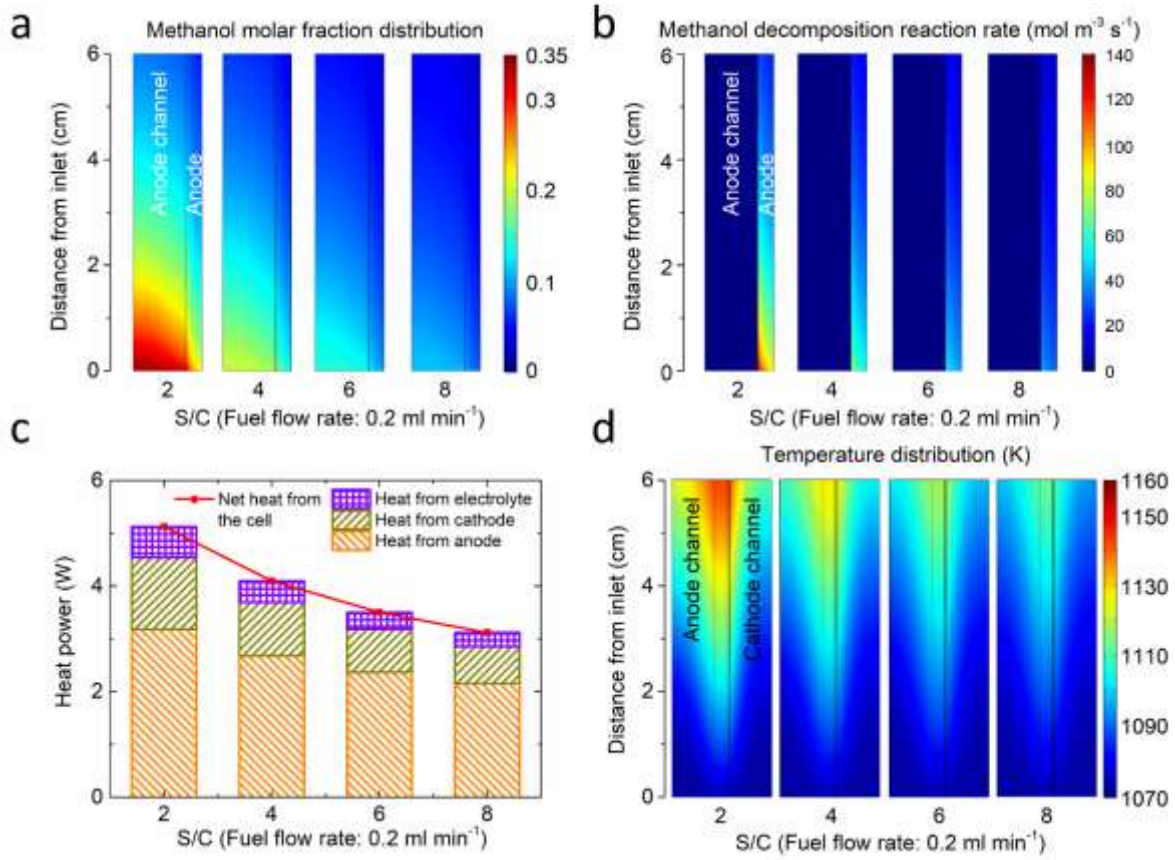

Fig. 6. The effects of the S/C ratio on: (a) methanol molar fraction; (b) MDR rate; (c) heat source of each component; (d) temperature distribution.

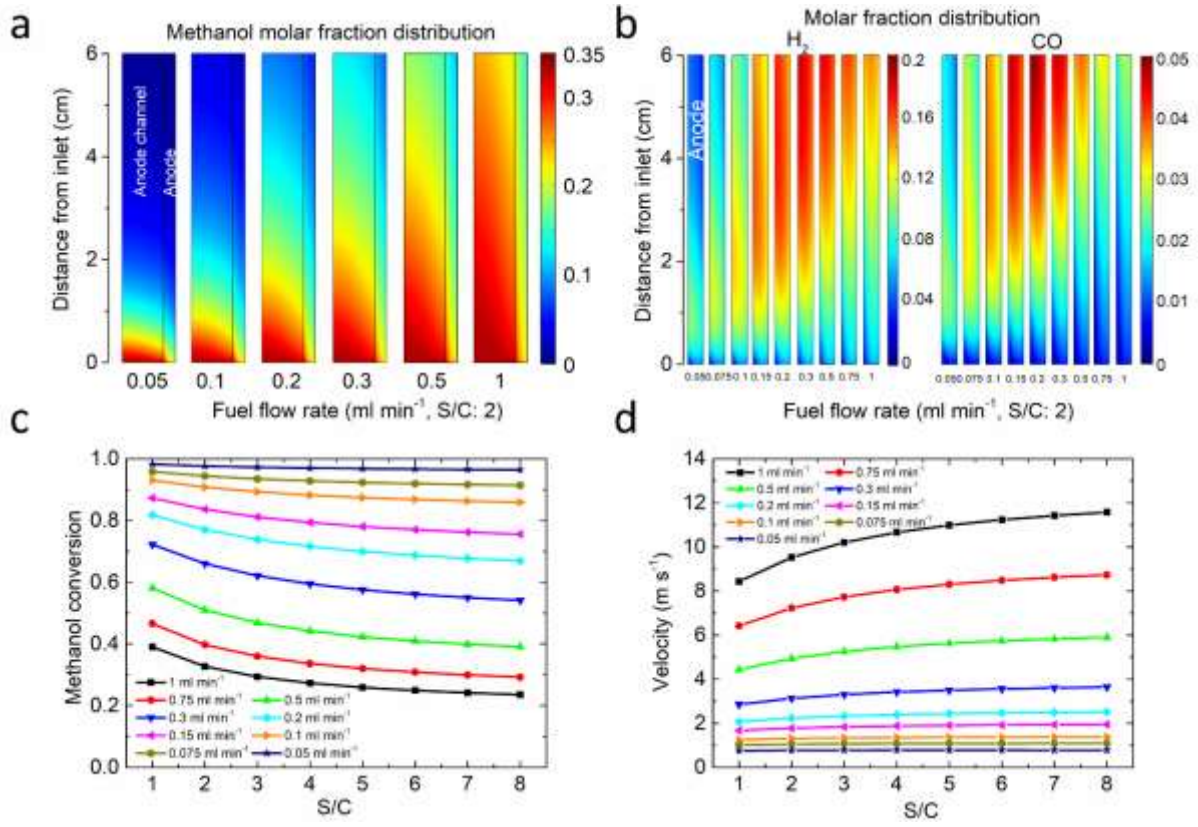

Fig. 7. The effects of fuel flow rate on: (a) methanol molar fraction; (b) hydrogen and carbon monoxide molar fractions; (c) methanol conversion; (d) the average velocity at the centre of the fuel channel.

Besides, the current densities can also be influenced by the fuel flow rate (Fig. 5). At a lower fuel flow rate, the methanol is almost exhausted (Fig. 7a), and the syngas is insufficient in the downstream for the electrochemical reactions, as shown in Fig. 7b. With increasing fuel flow rate, more methanol is supplied to produce more syngas, which will help increase the local equilibrium potential and thus local current density (Fig. 7b). However, as the fuel flow rate approaches 0.2 ml min^{-1}, the performance improvement becomes insignificant. A further increase in the flow rate to 1.0 ml min^{-1} could even decrease the cell performance (Fig. 5) as the high fuel flow rate can easily take away the produced CO and H_2, leading to lower CO/H_2 concentrations (Fig. 7b) and lower SOFC performance. Furthermore, the conversion is decreasing with increasing fuel flow rate (Fig. 7c), because at the higher velocity (Fig. 7d) there is more unreacted methanol flowing away the fuel channel (Fig. 7a), leading to lower efficiency of the fuel cell system. Also, an increase of the S/C ratio results in the drop of the methanol conversion (Fig. 7c), since a higher S/C ratio leads to a faster fuel gas mixture velocity (Fig. 7d). Moreover, It is also found that the enhancement of the current density by the effect of the fuel flow rate (less than 0.2 ml min^{-1}) is more significant at low S/C ratio (Fig. 5). This

phenomenon is caused by the fact that methanol molar fraction by increasing the fuel flow rate at small S/C ratio is much considerable than that at the higher S/C ratio (Fig. 8a), thus leading to larger performance improvement at a lower S/C ratio.

The fuel flow rate also plays a role in the temperature distribution within the whole cell. When the fuel flow rate increases from 0.05 ml min^{-1} to 0.1ml min^{-1}, the peak temperature near the outlet is found to increase because of the higher current density (Fig. 8b). However, there is a noticeable decrease of the peak temperature when the fuel flow rate further increases from 0.1 ml min^{-1}, which is mainly caused by the multi-effect of the faster flow rate. As just mentioned, the relatively higher fuel rate (less than 0.2 ml min^{-1}) can improve the performance of SOFC, so the total heat generation by electrochemical reactions and overpotential losses are accordingly increased. However, sufficient methanol benefits the endothermic methanol decomposition reaction, which is evidenced by the heat consumption shown in Fig. 8d. This can lead to a slight drop of the total heat generation of the whole cell as the fuel flow rate is increased from 0.15 ml min^{-1}, as shown in Fig. 8c. Therefore, the increase of the peak temperature with increasing fuel flow rate from 0.05 ml min^{-1} to 0.1ml min^{-1} indicates the higher heat generation than the heat consumption. When the fuel flow rate is increased from 0.1 ml min^{-1} to 0.15 ml min^{-1}, the faster flow velocity (Fig. 7d) in the fuel channel takes away more heat by convection leading to the decrease of the peak temperature although the total heat is still increasing. Both faster fuel flow velocity and the drop of the total heat generation decrease the peak temperature, when the fuel flow rate increases from 0.15 ml min^{-1}.

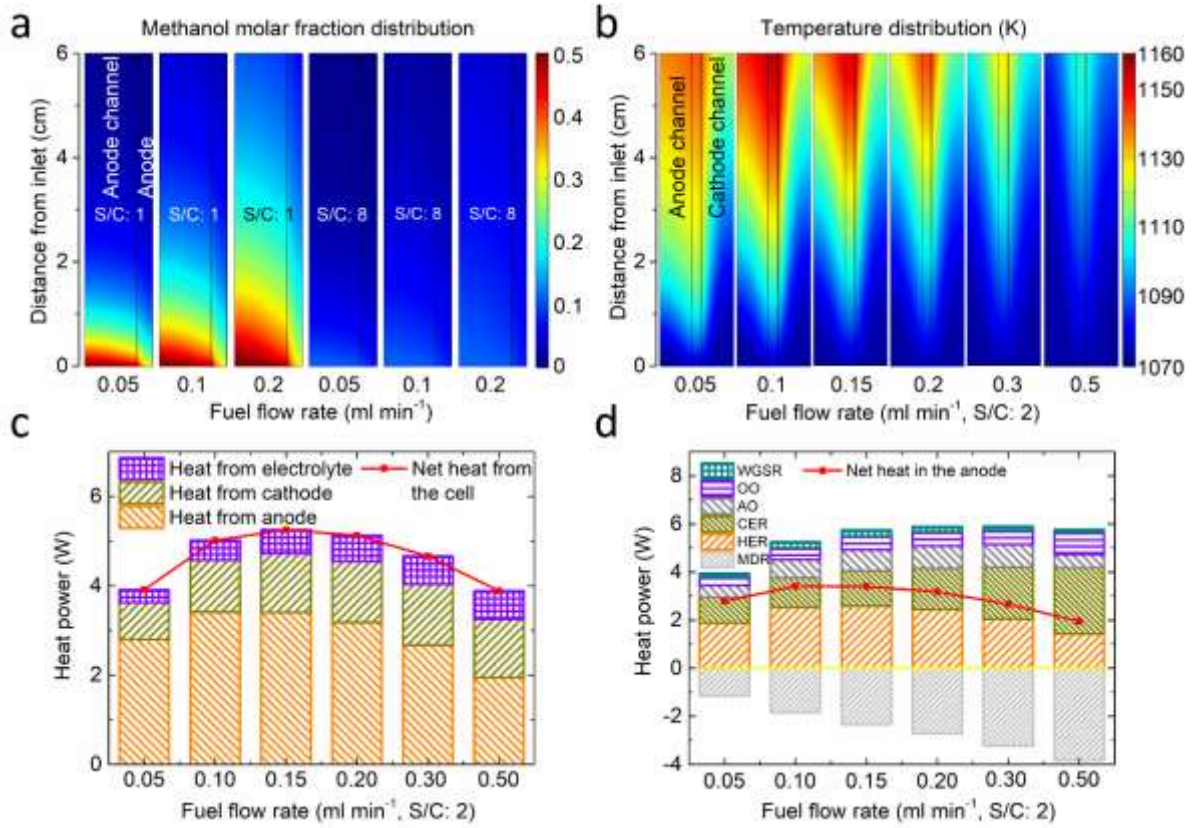

Fig. 8. (a) effects of fuel flow rate and different S/C ratio on methanol molar fractions; The effects of fuel flow rate on: (b) temperature distribution; (c) heat source of each component; (d) heat source of the anode.

3.3 The effects of the air flow rate

The air flow rate is another essential parameter for the SOFC operation. Simulations are performed under various air flow rates and different S/C ratios at an inlet temperature of 1073 K, fuel flow rate of 0.2 ml min^{-1} and the operating potential of 0.6 V.

As can be seen from Fig. 9a, the computed current densities increase very significantly with increasing air flow rate, especially at an air flow rate of below 200 SCCM. At an air flow rate of between 10 and 160 SCCM, the current densities curves show same changes at different S/C ratios as the SOFC performance is limited by the low oxygen concentration in the cathode, especially in the downstream (Fig. 9b). When the air flow rate exceeds 200 SCCM, the oxygen supply is sufficient and the anode gas composition determines the performance, causing different current densities under different S/C ratios (Fig. 9a). From Fig. 9c, the average temperature of each component is also greatly affected by the air flow rate. Due to the significantly increased current density and thus increased heat generation (orange line in Fig. 9c) with increasing air flow rate, the average temperature of each component is found to increase as the air flow rate is increased from 10 to about 170 SCCM. However, further increase

in air flow rate cause the average temperatures to decrease as the fast air flow can easily take away the generated heat (Fig. 9d). The largest temperature drop occurs in air channel (olive line in Fig. 9c), thereby leading to the drop of the cell temperature, which is in consistence with the temperature distributions in Fig. 10. Normally, active cooling of the cell is achieved by the oversupply of the air into the cathode channel [63], increasing energy consumption for heating air and thus the operating cost of the SOFC. Fig. 10 shows the temperature distribution under various air flow rates. The peak temperature is found at the middle of the cell and the temperature decreases along the cell length from the peak temperature area at lower air flow rates, mainly due to the exhausted oxygen (Fig. 9b) and endothermic decomposition reaction. At higher air flow rate, the temperature increases along the cell length and the peak temperature occurs at the outlet of the cell, which is caused by the fact that the exothermic processes are greatly enhanced.

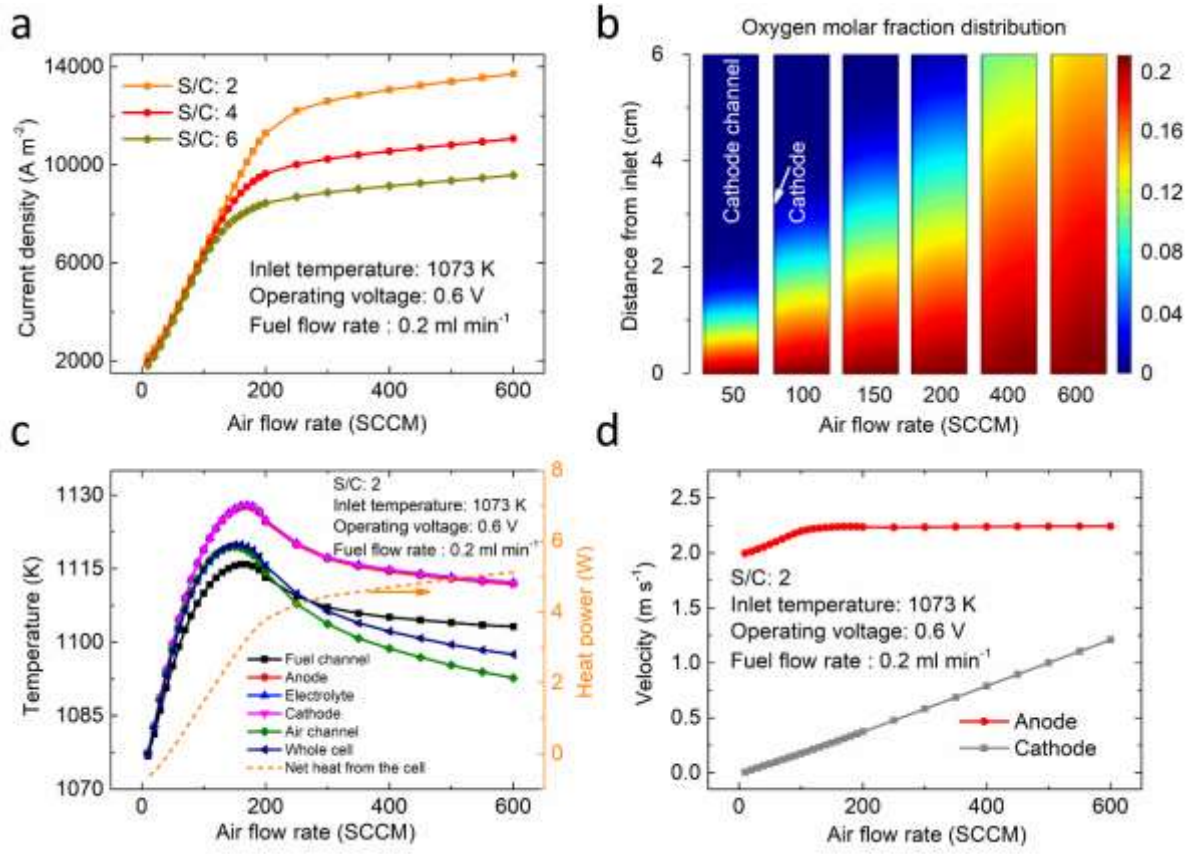

Fig. 9. The effects of the air flow rate on: (a) current density; (b) oxygen molar fraction; (c) average temperature of each component; (d) average velocities at the center of the fuel and air channels, respectively

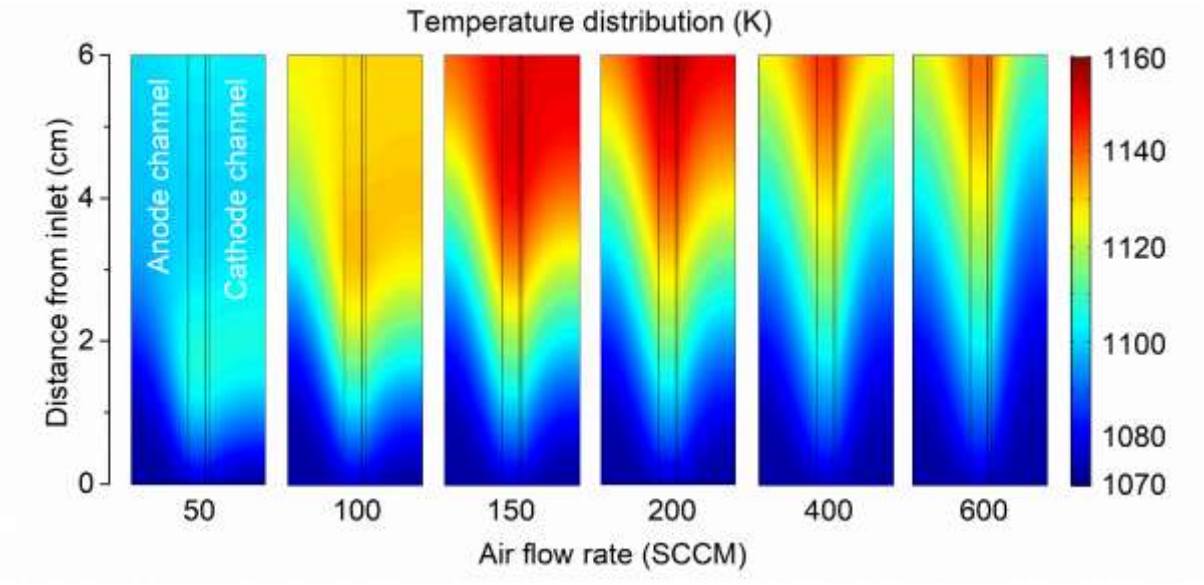

Fig. 10. The effect of the air flow rate on temperature distribution.

3.4 The effects of the inlet temperature

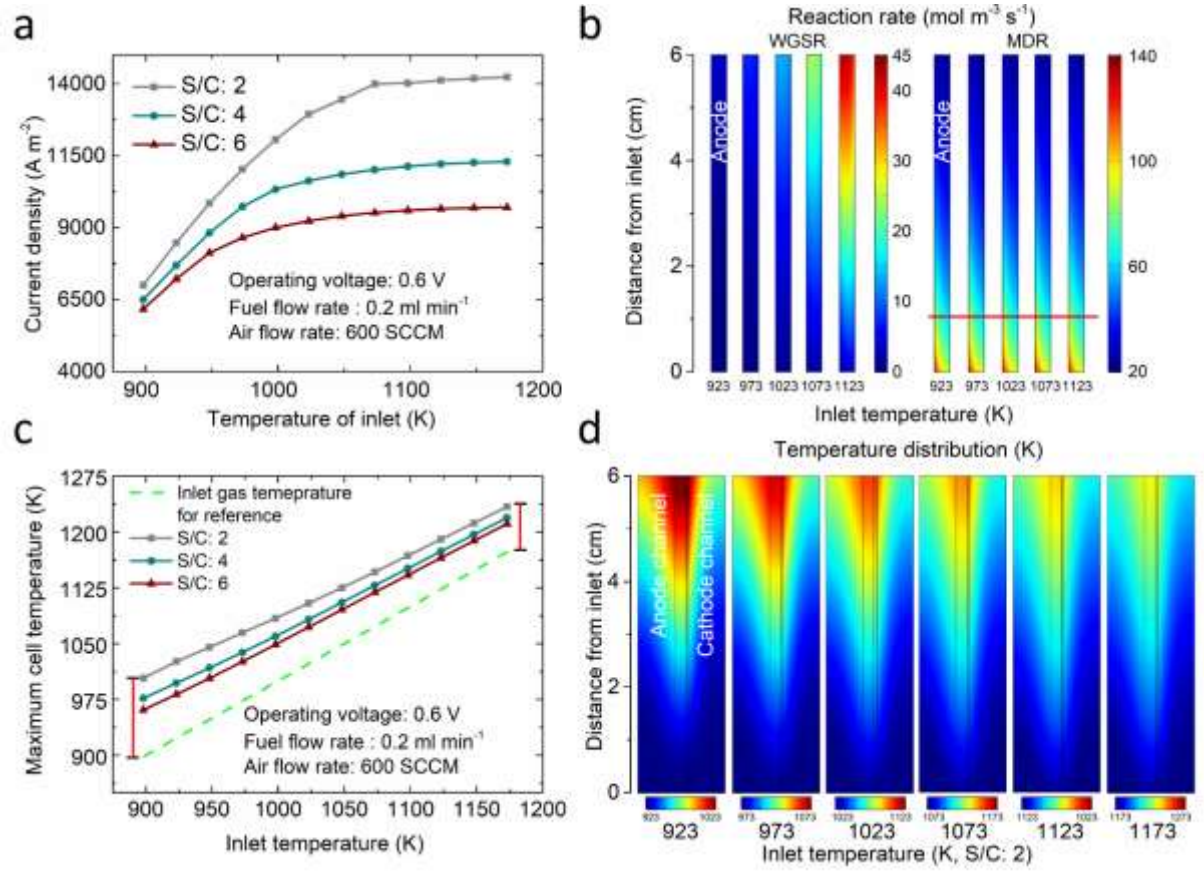

Fig. 11. The effects of the inlet temperature on: (a) current density; (b) rates of the WGSR and MDR; (c) maximum temperature in the SOFC; (d) temperature distribution.

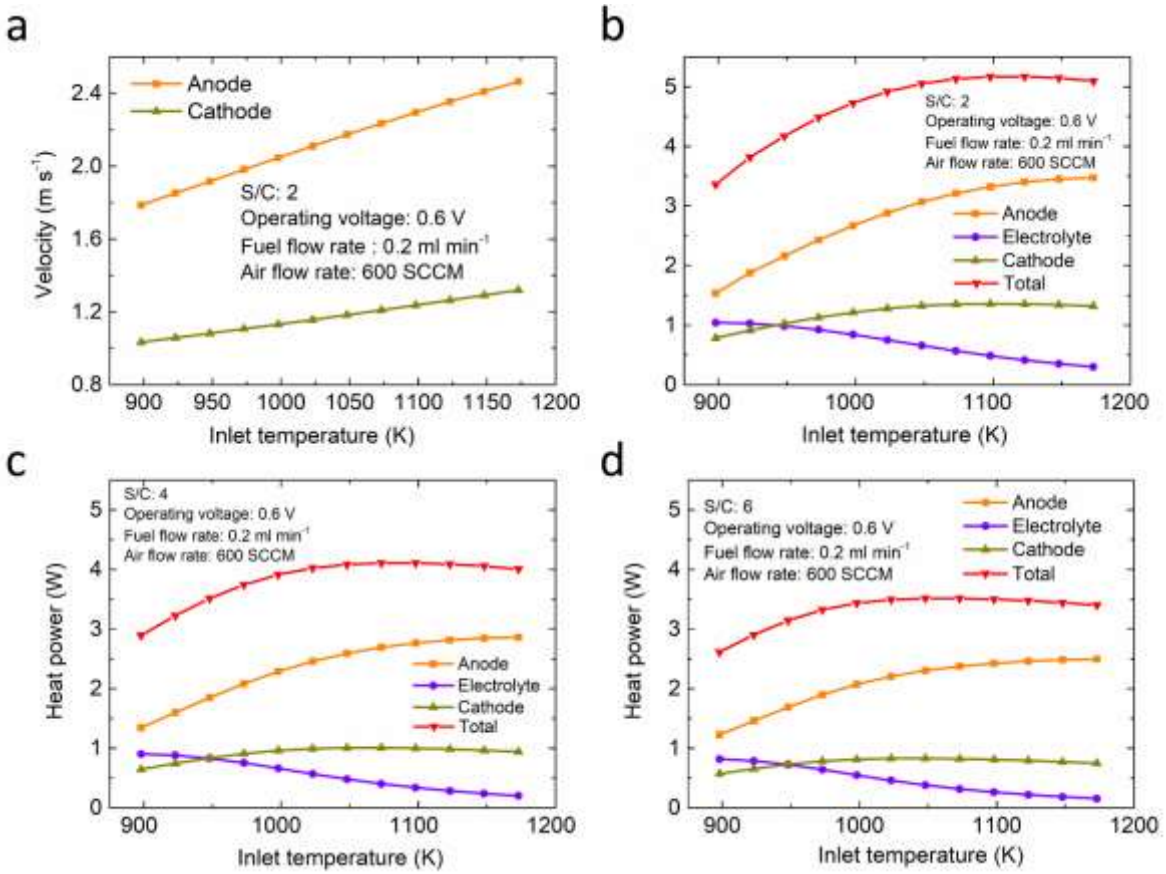

Fig. 12. The effects of the inlet temperature on: (a) average velocities at the centre of the fuel and air channels; (b) heat source of each component at S/C ratio of 2; (c) heat source of each component at S/C ratio of 4; (d) heat source of each component at S/C ratio of 6.

The temperature of the inlet has great impacts on not only the reactions involved in the SOFC but also the properties of the materials and the gas species. In addition, because of the complex endothermic and exothermic processes, the average cell temperature could be substantially different from the inlet temperature. Therefore, in this section, simulations are conducted to study the effects of the inlet gas temperature on SOFC performance under several S/C ratios at a potential of 0.6 V, and fuel and air flow rates of 0.2 ml min^{-1} and 600 SCCM, respectively.

As expected, the simulated current densities are found to increase when the inlet temperature is changing from 893 K to 1173 K (Fig. 11a) because the higher rates of the chemical/electrochemical reactions and the higher ion conductivity at a higher operating temperature. Highly increased water gas shift reaction rate and slightly increased methanol decomposition rate tend to produce more direct fuels for power generation (Fig. 11b). Although the maximum temperature increases with increasing inlet temperature, the difference between the maximum temperature and the inlet temperature becomes smaller (Fig. 11c) due to the combined effect of the faster gas velocities in fuel and air channels (Fig. 12a) and the slower

rise or even slight drop of the total heat generation when the inlet gas temperature is increasing (Fig. 12b, c and d), enhancing the temperature uniformity (Fig. 11d). Generally, after the significant increase at the beginning of the temperature rise, the total heat generation faces a decline from 1073 K for both S/C ratios of 4 (Fig. 12c) and 6 (Fig. 12d), and from 1123 K for a S/C ratio of 2 (Fig. 12b). The slight decrease of the heat generation at high inlet gas temperature is mainly because the drop of heat power generated from the electrolyte (Eq. (52)) caused by the improved ionic conductivity of the ceramic electrolyte, could overcome the increases of the heat generations from anode and cathode even though the current densities are continuing improved (Fig. 11a). It is also obviously observed that the porous anode contributes most to the total heat generation, which is mainly caused by the irreversible entropy changes of the H_2 and CO electrochemical reactions at a higher current density (Eq. (51)).

4 Conclusions

A mathematic model is established to examine the thermal characteristics of the tubular methanol-fuelled SOFC with the addition of the adequate steam into the fuel stream to suppress carbon deposition. The model fully considers the thermal coupling of the endothermic methanol decomposition reaction with the cell inefficiencies, investigating the influences of various essential operating parameters, involving applied potential, inlet gas temperature, steam to carbon ratio, as well as the fuel and gas flow rates. Performance and the thermal effect indicators, including current density, temperature distribution, gas molar fraction, chemical reactions rate etc. are comprehensively discussed in parametric simulations.

Peak power density of 10220 W m^{-2} is attained when the fuel mixture with equal molar amounts of steam and methanol is fed into the SOFC at 0.55 V and 1073 K. Stagnant methanol conversion and the nearly exhausted synthesis gas cause slight drop of the current density as the voltage further decreases from 0.45 V. Higher S/C ratio tends to dilute the methanol fuel and the generated syngas, leading to the reductions in the electricity power and the total heat generation. It is found that increasing the fuel (less than 0.2 ml min^{-1}) or air flow rates improves the performance of the SOFC, and it also serves as a cooling strategy for the temperature control of the cell. However, side effects of the higher fuel and air flow rates are the lower fuel conversion and the additional energy input, which could negatively affect the efficiency of the whole system. The rise of the inlet temperature from 898 K to 1173 K significantly enhances the power performance due to higher syngas production rates, higher ion conduction through the electrolyte, and higher electrochemical reaction kinetics of the electrodes at elevated inlet temperature. Meanwhile, the improved ion conduction and electrode reaction kinetics also contribute to the reduction of the heat generation, leading to more uniform temperature

distribution. Overall, the results of the current study provide insightful information on the thermal characteristics of the high temperature methanol-fuelled SOFCs, which are critical for the performance and durability of SOFC.

Acknowledgement

M. Ni thanks the funding support (Project Number: PolyU 152064/18E) from Research Grant Council, University Grants Committee, Hong Kong SAR.

References

[1] Singhal SC, Kendall K. High-temperature Solid Oxide Fuel Cells: Fundamentals, Design and Applications. Amsterdam, Netherlands: Elsevier; 2003. https://doi.org/10.1016/B978-1-85617-387-2.X5016-8.

[2] McIntosh S, Gorte RJ. Direct hydrocarbon solid oxide fuel cells. Chem Rev 2004;104:4845–65. https://doi.org/10.1021/cr020725g.

[3] Badwal SPS, Giddey S, Kulkarni A, Goel J, Basu S. Direct ethanol fuel cells for transport and stationary applications - A comprehensive review. Appl Energy 2015;145:80–103. https://doi.org/10.1016/j.apenergy.2015.02.002.

[4] Cinti G, Desideri U, Penchini D, Discepoli G. Experimental analysis of SOFC fuelled by ammonia. Fuel Cells 2014;14:221–30. https://doi.org/10.1002/fuce.201300276.

[5] Murray EP, Harris SJ, Jen H. Solid Oxide Fuel Cells Utilizing Dimethyl Ether Fuel. J Electrochem Soc 2002;149:A1127. https://doi.org/10.1149/1.1496484.

[6] Jiang Y, Virkar A V. A High Performance, Anode-Supported Solid Oxide Fuel Cell Operating on Direct Alcohol. J Electrochem Soc 2001;148:A706. https://doi.org/10.1149/1.1375166.

[7] Bai Y, Liu Y, Tang Y, Xie Y, Liu J. Direct carbon solid oxide Fuel Cell - A potential high performance battery. Int J Hydrogen Energy 2011;36:9189–94. https://doi.org/10.1016/j.ijhydene.2011.04.171.

[8] Radenahmad N, Azad AT, Saghir M, Taweekun J, Bakar MSA, Reza MS, et al. A review on biomass derived syngas for SOFC based combined heat and power application. Renew Sustain Energy Rev 2020;119:109560. https://doi.org/10.1016/j.rser.2019.109560.

[9] Xu H, Chen B, Liu J, Ni M. Modeling of direct carbon solid oxide fuel cell for CO and electricity cogeneration. Appl Energy 2016;178:353–62. https://doi.org/10.1016/j.apenergy.2016.06.064.

[10] Ni M, Shao ZP. Fuel cells that operate at 300º to 500ºC. Science 2020; 369(6500): 138-139. DOI: 10.1126/science.abc9136.

[11] Ni M, Leung DYC, Leung MKH. A review on reforming bio-ethanol for hydrogen production. Int J Hydrogen Energy 2007;32:3238–47. https://doi.org/10.1016/j.ijhydene.2007.04.038.

[12] Olah GA. Beyond oil and gas: The methanol economy. Angew Chemie - Int Ed 2005;44:2636–9. https://doi.org/10.1002/anie.200462121.

[13] Park S, Vohs JM, Gorte RJ. Direct oxidation of hydrocarbons in a solid-oxide fuel cell.

Nature 2000;404:265–7. https://doi.org/10.1038/35005040.

[14] Cimenti M, Alzate-Restrepo V, Hill JM. Direct utilization of methanol on impregnated Ni/YSZ and Ni-Zr0.35Ce0.65O2/YSZ anodes for solid oxide fuel cells. J Power Sources 2010;195:4002–12. https://doi.org/10.1016/j.jpowsour.2009.12.119.

[15] Lo Faro M, Stassi A, Antonucci V, Modafferi V, Frontera P, Antonucci P, et al. Direct utilization of methanol in solid oxide fuel cells: An electrochemical and catalytic study. Int J Hydrogen Energy 2011;36:9977–86. https://doi.org/10.1016/j.ijhydene.2011.05.053.

[16] Palo DR, Dagle RA, Holladay JD. Methanol steam reforming for hydrogen production. Chem Rev 2007;107:3992–4021. https://doi.org/10.1021/cr050198b.

[17] Cimenti M, Hill JM. Thermodynamic analysis of solid oxide fuel cells operated with methanol and ethanol under direct utilization, steam reforming, dry reforming or partial oxidation conditions. J Power Sources 2009;186:377–84. https://doi.org/10.1016/j.jpowsour.2008.10.043.

[18] Park N, Park MJ, Ha KS, Lee YJ, Jun KW. Modeling and analysis of a methanol synthesis process using a mixed reforming reactor: Perspective on methanol production and CO2 utilization. Fuel 2014;129:163–72. https://doi.org/10.1016/j.fuel.2014.03.068.

[19] Son M, Woo Y, Kwak G, Lee YJ, Park MJ. CFD modeling of a compact reactor for methanol synthesis: Maximizing productivity with increased thermal controllability. Int J Heat Mass Transf 2019;145:118776. https://doi.org/10.1016/j.ijheatmasstransfer.2019.118776.

[20] Leonzio G, Foscolo PU. Analysis of a 2-D model of a packed bed reactor for methanol production by means of CO2 hydrogenation. Int J Hydrogen Energy 2020;45:10648–63. https://doi.org/10.1016/j.ijhydene.2020.01.248.

[21] Wang W, Su C, Wu Y, Ran R, Shao Z. Progress in solid oxide fuel cells with nickel-based anodes operating on methane and related fuels. Chem Rev 2013;113:8104–51. https://doi.org/10.1021/cr300491e.

[22] Liu M, Peng R, Dong D, Gao J, Liu X, Meng G. Direct liquid methanol-fueled solid oxide fuel cell. J Power Sources 2008;185:188–92. https://doi.org/10.1016/j.jpowsour.2008.06.076.

[23] Meng X, Zhan Z, Liu X, Wu H, Wang S, Wen T. Low-temperature ceria-electrolyte solid oxide fuel cells for efficient methanol oxidation. J Power Sources 2011;196:9961–4. https://doi.org/10.1016/j.jpowsour.2011.08.002.

[24] Lin Y, Zhan Z, Liu J, Barnett SA. Direct operation of solid oxide fuel cells with methane

fuel. Solid State Ionics 2005;176:1827–35. https://doi.org/10.1016/j.ssi.2005.05.008.

[25] Cimenti M, Hill JM. Importance of pyrolysis and catalytic decomposition for the direct utilization of methanol in solid oxide fuel cells. J Power Sources 2010;195:54–61. https://doi.org/10.1016/j.jpowsour.2009.07.007.

[26] Jeon OS, Lee JG, Ji Y, Lee SH, Kwon O, Kim JP, et al. Effects of dispersed copper nanoparticles on Ni-ceria based dry methanol fuelled low temperature solid oxide fuel cells. RSC Adv 2019;9:6320–7. https://doi.org/10.1039/c8ra07586g.

[27] Jang DY, Koo J, Choi HR, Kim JW, Jeong HJ, Prinz FB, et al. Coke-Free Oxidation of Methanol in Solid Oxide Fuel Cells with Heterogeneous Nickel-Palladium Catalysts Prepared by Atomic Layer Deposition. ACS Sustain Chem Eng 2020;8:10529–35. https://doi.org/10.1021/acssuschemeng.0c03020.

[28] Li P, Yu B, Li J, Yao X, Zhao Y, Li Y. Improved activity and stability of Ni-Ce0.8Sm0.2O1.9 anode for solid oxide fuel cells fed with methanol through addition of molybdenum. J Power Sources 2016;320:251–6. https://doi.org/10.1016/j.jpowsour.2016.04.100.

[29] Ding G, Gan T, Yu J, Li P, Yao X, Hou N, et al. Carbon-resistant Ni1-xCox-Ce0.8Sm0.2O1.9 anode for solid oxide fuel cells fed with methanol. Catal Today 2017;298:250–7. https://doi.org/10.1016/j.cattod.2017.03.060.

[30] Li P, Fang L, Hou N, Li J, Yao X, Gan T, et al. Improved Performance of Ni-Mo Based Anode for Direct Methanol Solid Oxide Fuel Cells with the Addition of Rare Earth Oxides. J Electrochem Soc 2017;164:F1142–8. https://doi.org/10.1149/2.1021712jes.

[31] Yao X, Fan L, Gan T, Hou N, Li P, Zhao Y, et al. Coking-resistant NbOx-Ni-Ce0.8Sm0.2O1.9 anode material for methanol-fueled solid oxide fuel cells. Int J Hydrogen Energy 2018;43:12748–55. https://doi.org/10.1016/j.ijhydene.2018.03.186.

[32] Li P, Wang R, Yan F. Effect of Pr addition into Ni based anode on direct methanol fueled solid oxide fuel cell. J Electroanal Chem 2020;859:113846. https://doi.org/10.1016/j.jelechem.2020.113846.

[33] Gao Z, Raza R, Zhu B, Mao Z. Development of methanol-fueled low-temperature solid oxide fuel cells. Int J Energy Res 2011;35:690–6. https://doi.org/10.1002/er.1718.

[34] Laosiripojana N, Assabumrungrat S. Catalytic steam reforming of methane, methanol, and ethanol over Ni/YSZ: The possible use of these fuels in internal reforming SOFC. J Power Sources 2007;163:943–51. https://doi.org/10.1016/j.jpowsour.2006.10.006.

[35] Ru Y, Sang J, Xia C, Wei WCJ, Guan W. Durability of direct internal reforming of methanol as fuel for solid oxide fuel cell with double-sided cathodes. Int J Hydrogen

Energy 2020;45:7069–76. https://doi.org/10.1016/j.ijhydene.2019.12.222.

[36] Chen B, Xu H, Tan P, Zhang Y, Xu X, Cai W, et al. Thermal modelling of ethanol-fuelled Solid Oxide Fuel Cells. Appl Energy 2019;237:476–86. https://doi.org/10.1016/j.apenergy.2019.01.025.

[37] Cimenti M, Hill JM. Direct utilization of liquid fuels in SOFC for portable applications: Challenges for the selection of alternative anodes. Energies 2009;2:377–410. https://doi.org/10.3390/en20200377.

[38] Khan MS, Lee SB, Song RH, Lee JW, Lim TH, Park SJ. Fundamental mechanisms involved in the degradation of nickel–yttria stabilized zirconia (Ni–YSZ) anode during solid oxide fuel cells operation: A review. Ceram Int 2016;42:35–48. https://doi.org/10.1016/j.ceramint.2015.09.006.

[39] Xu Q, Ni M. Modelling of high temperature direct methanol solid oxide fuel cells. Int J Energy Res 2020:1–16. https://doi.org/10.1002/er.6003.

[40] Shi Y, Li C, Cai N. Experimental characterization and mechanistic modeling of carbon monoxide fueled solid oxide fuel cell. J Power Sources 2011;196:5526–37. https://doi.org/10.1016/j.jpowsour.2011.02.013.

[41] Ni M. Modeling and parametric simulations of solid oxide fuel cells with methane carbon dioxide reforming. Energy Convers Manag 2013;70:116–29. https://doi.org/10.1016/j.enconman.2013.02.008.

[42] Mizsey P, Newson E, Truong T binh, Hottinger P. The kinetics of methanol decomposition: A part of autothermal partial oxidation to produce hydrogen for fuel cells. Appl Catal A Gen 2001;213:233–7. https://doi.org/10.1016/S0926-860X(00)00907-8.

[43] Haberman BA, Young JB. Three-dimensional simulation of chemically reacting gas flows in the porous support structure of an integrated-planar solid oxide fuel cell. Int J Heat Mass Transf 2004;47:3617–29. https://doi.org/10.1016/j.ijheatmasstransfer.2004.04.010.

[44] Ni M. Modeling of SOFC running on partially pre-reformed gas mixture. Int J Hydrogen Energy 2012;37:1731–45. https://doi.org/10.1016/j.ijhydene.2011.10.042.

[45] Ni M. An electrochemical model for syngas production by co-electrolysis of H 2 O and CO 2. J Power Sources 2012;202:209–16. https://doi.org/10.1016/j.jpowsour.2011.11.080.

[46] Xu H, Chen B, Zhang H, Kong W, Liang B, Ni M. The thermal effect in direct carbon solid oxide fuel cells. Appl Therm Eng 2017.

https://doi.org/10.1016/j.applthermaleng.2017.03.027.

[47] Coker AK. Ludwig's Applied Process Design for Chemical and Petrochemical Plants. Gulf Prof Publ 2007. https://doi.org/10.1016/B978-0-7506-7766-0.X5000-3.

[48] Krishna R, Wesselingh JA. The Maxwell-Stefan approach to mass tranfer. Chem Eng Sci 1997;52:861–911. https://doi.org/10.1016/S0009-2509(96)00458-7.

[49] Vural Y, Ma L, Ingham DB, Pourkashanian M. Comparison of the multicomponent mass transfer models for the prediction of the concentration overpotential for solid oxide fuel cell anodes. J Power Sources 2010;195:4893–904. https://doi.org/10.1016/j.jpowsour.2010.01.033.

[50] Evans RB, Watson GM, Mason EA. Gaseous diffusion in porous media at uniform pressure. J Chem Phys 1961;35:2076–83. https://doi.org/10.1063/1.1732211.

[51] Todd B, Young JB. Thermodynamic and transport properties of gases for use in solid oxide fuel cell modelling. J Power Sources 2002;110:186–200. https://doi.org/10.1016/S0378-7753(02)00277-X.

[52] Veldsink JW, van Damme RMJ, Versteeg GF, van Swaaij WPM. The use of the dusty-gas model for the description of mass transport with chemical reaction in porous media. Chem Eng J Biochem Eng J 1995;57:115–25. https://doi.org/10.1016/0923-0467(94)02929-6.

[53] Poling BE, Prausnitz JM, O'Connell JP, Reid RC, Sherwood TK, Street RE. The properties of gases and liquids. vol. 12. 2001. https://doi.org/10.1063/1.3060771.

[54] Fuller EN, Ensley K, Giddings JC. Diffusion of halogenated hydrocarbons in helium. The effect of structure on collision cross sections. J Phys Chem 1969;73:3679–85. https://doi.org/10.1021/j100845a020.

[55] Luo Y, Shi Y, Li W, Cai N. Comprehensive modeling of tubular solid oxide electrolysis cell for co-electrolysis of steam and carbon dioxide. Energy 2014;70:420–34. https://doi.org/10.1016/j.energy.2014.04.019.

[56] He Q, Yu J, Xu H, Zhao D, Zhao T, Ni M. Thermal effects in H2O and CO2 assisted direct carbon solid oxide fuel cells. Int J Hydrogen Energy 2020;45:12459–75. https://doi.org/10.1016/j.ijhydene.2020.02.169.

[57] Wiranarongkorn K, Banerjee A, Deutschmann O, Arpornwichanop A. Performance analysis and temperature gradient of solid oxide fuel cell stacks operated with bio-oil sorption-enhanced steam reforming. Int J Hydrogen Energy 2020;45:12108–20. https://doi.org/10.1016/j.ijhydene.2020.02.120.

[58] Neelakandan S, Liu D, Wang L, Hu M, Wang L. Highly branched poly(arylene

ether)/surface functionalized fullerene-based composite membrane electrolyte for DMFC applications. Int J Energy Res 2019;43:3756–67. https://doi.org/10.1002/er.4536.

[59] Munjewar SS, Thombre SB, Mallick RK. Approaches to overcome the barrier issues of passive direct methanol fuel cell – Review. Renew Sustain Energy Rev 2017;67:1087–104. https://doi.org/10.1016/j.rser.2016.09.002.

[60] Wang Y, Zhan R, Qin Y, Zhang G, Du Q, Jiao K. Three-dimensional modeling of pressure effect on operating characteristics and performance of solid oxide fuel cell. Int J Hydrogen Energy 2018;43:20059–76. https://doi.org/10.1016/j.ijhydene.2018.09.025.

[61] Liu X, Martin CL, Bouvard D, Di Iorio S, Laurencin J, Delette G. Strength of highly porous ceramic electrodes. J Am Ceram Soc 2011;94:3500–8. https://doi.org/10.1111/j.1551-2916.2011.04669.x.

[62] Yakabe H, Baba Y, Sakurai T, Yoshitaka Y. Evaluation of the residual stress for anode-supported SOFCs. J Power Sources 2004;135:9–16. https://doi.org/10.1016/j.jpowsour.2003.11.049.

[63] Boldrin P, Brandon NP. Progress and outlook for solid oxide fuel cells for transportation applications. Nat Catal 2019;2:571–7. https://doi.org/10.1038/s41929-019-0310-y.